CHAPTER 4

RESULTS AND DISCUSSION

4.1 ZnTe by microwave plasma

Figure 4.1 are the representative XRD pattern of the products. All spectra of the products were characterized using XRD and JCPDS database (Reference codes: 15-0746 for ZnTe, 01-1238 for Zn, and 01-0714 for Te) [70]. At 1:1 molar ratio of Zn:Te and under the 10, 20 and 30 min conditions, the products (10, 20 and 30 min) were composed of ZnTe with some impurities. For 10 min long reaction time, both Zn and Te impurities were left in the product. When the reaction time was lengthened to 20 and 30 min, only Te impurity was left in the main products. No such impurities were detected, when the experimental time was lengthened to 40 min. At the present stage, the chemical reaction of Zn and Te was complete, and only cubic ZnTe was produced as the main product. The sharp peaks indicated good crystallization of ZnTe. The strongest intensity peak is at $2\theta = 25.236$ degrees and diffracts from the (111) planes of the products.

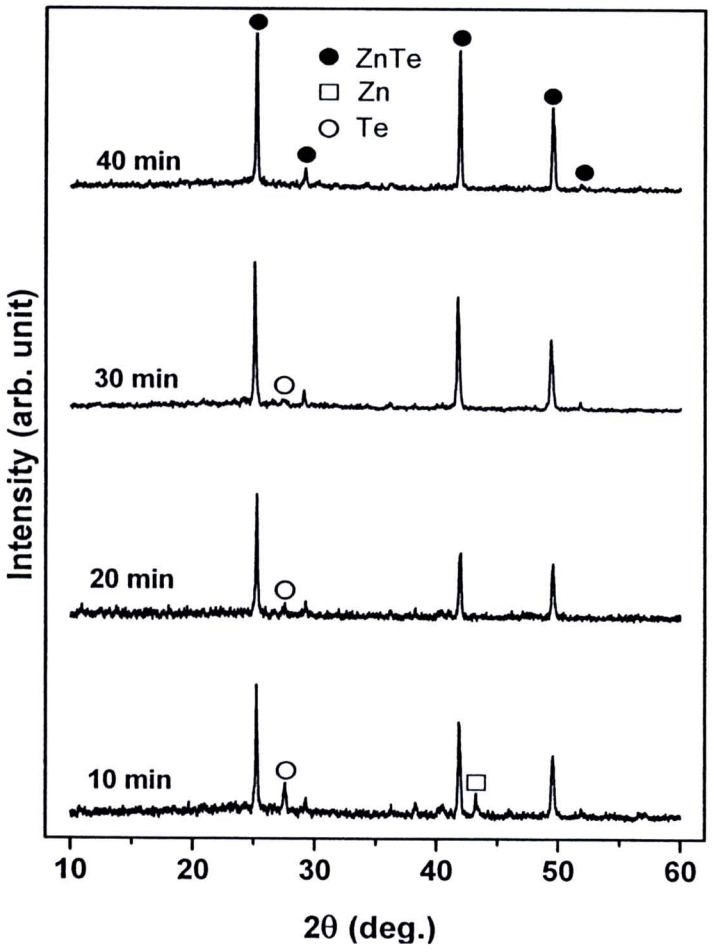

Figure 4.1 XRD spectra of the products prepared using 1:1 molar ratio of Zn:Te.

The interplanar spacings (*d*) and lattice parameters (*a*) of different diffraction peaks of the 1:1 molar ratio Zn:Te product were calculated using Bragg's law for diffraction, and the plane-spacing equation for cubic structure [71]. These d spaces of different planes and average lattice parameter (a = 6.1004±0.0041 Å) (Table 4.1) are in good accordance with those of the JCPDS standard [70].

Table 4.1 Calculated lattice parameter of ZnTe from the experiment (molar ratio of Zn:Te = 1:1, 40 min.) comparing with the JCPDS file (Reference code: 15-0746 for ZnTe)

Plane	2θ, Exp. (deg.)	2θ, JCPDS file (deg.)	Interplanar spacing (d), (Exp.) Å	Interplanar Spacing (d) JCPDS file, Å	Lattice parameter, (Exp.) Å	Lattice parameter JCPDS file, Å
(111)	25.236	25.259	3.5248	3.5230	6.1052	6.1026
(200)	29.230	29.248	3.0516	3.0510	6.1033	6.1026
(220)	41.868	41.806	2.1551	2.1590	6.0956	6.1026
(311)	49.528	49.498	1.8383	1.8400	6.0968	6.1026
(222)	51.85	51.847	1.7613	1.7620	6.1012	6.1026
					6.1004±0.0041	

Figure 4.2 is the representative XRD patterns of ZnTe samples at molar ratio of 1.5:1 Zn:Te. At 1.5:1 molar ratio of Zn:Te and under the 10, 20 and 30 min conditions, the products (10, 20 and 30 min) were composed of ZnTe with some impurities of Zn and Te raw materials. For 10 min long, both Zn and Te impurities were left in the product. When the reaction time was lengthened to 20 and 30 min, Zn impurity was still left in the main products. No such impurities were detected, when the experimental time was lengthened to 40 min. This result of reaction time resemble the 1:1 molar ratio of Zn:Te condition, By using the 1.5:1 molar ratio of Zn:Te, Zn impurity was detected for the length of time of not more than 30 min, but the 1:1

molar ratio of Zn:Te condition, it was not more than 10 min, due to the increase of molar ratio of Zn as the reactant.

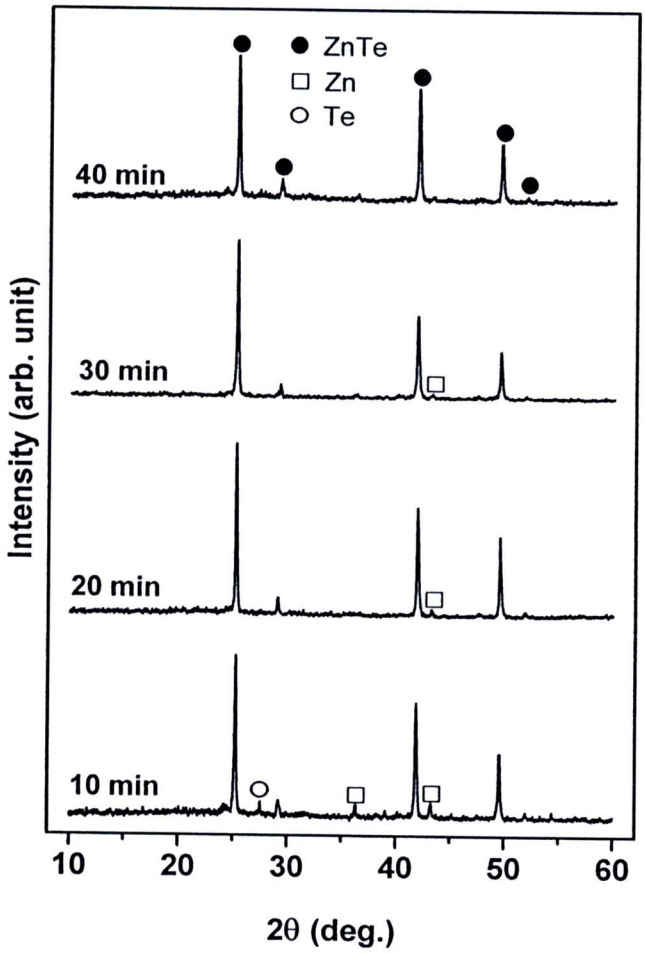

Figure 4.2 XRD spectra of the products prepared using 1.5:1 molar ratio of Zn:Te.

The interplanar spacings (*d*) and lattice parameters (*a*) of different diffraction peaks of the 1.5:1 molar ratio of Zn:Te products were calculated using Bragg's law for diffraction, and the plane-spacing equation for cubic structure [71]. These d-spacings of different planes and average lattice parameter (a = 6.0992±0.0036 Å) (Table 4.2) are in good accordance with that of the JCPDS standard [70].

Table 4.2 Calculated lattice parameter of ZnTe from the experiment (molar ratio of Zn:Te = 1.5:1, 40 min.) comparing with the JCPDS file (Reference code: 15-0746 for ZnTe)

Plane	2θ, Exp. (deg.)	2θ, JCPDS file (deg.)	Interplanar spacing (d), (Exp.) Å	Interplanar Spacing (d) JCPDS file, Å	Lattice parameter, (Exp.) Å	Lattice parameter JCPDS file, Å
(111)	25.240	25.259	3.5243	3.5230	6.1042	6.1026
(200)	29.240	29.248	3.0506	3.0510	6.1012	6.1026
(220)	41.856	41.806	2.1557	2.1590	6.0972	6.1026
(311)	49.514	49.498	1.8387	1.8400	6.0984	6.1026
(222)	51.908	51.847	1.7594	1.7620	6.0948	6.1026
					6.0992±0.0036	

Figure 4.3 presents on how to save the energy consumption. The 1.8:1 molar ratio of Zn:Te was used in the process. ZnTe and some Zn impurity were detected in the product produced under the 10 min condition. When the experimental time was lengthened to 20 min, only ZnTe existed as the main products with no impurity detection. During the heating process, some of Zn and Te could evaporate as well. The interplanar spacings (d) and lattice parameters (a) of different diffraction peaks of 1.8:1 molar ratio of Zn:Te product were calculated using Bragg's law for diffraction, and the plane-spacing equation for cubic structure [71]. These d-spacings of different planes and average lattice parameter (a = 6.0977 ± 0.0023 Å) (Table 4.3) are in good accordance with that of the JCPDS standard [70]. Rate of reaction depend on

concentration of reactants [72], therefore increasing of Zn has affected to increase the driving force of the reaction, which promotes the reaction rate to become faster. Therefore, all conditions of the 1:1, 1.5:1 and 1.8:1 molar ratios of ZnTe, the values of 2θ diffraction angle, interplanar spacing (d), and lattice parameter obtained from the experiment are very close to those of the JCPDS standard for cubic ZnTe.

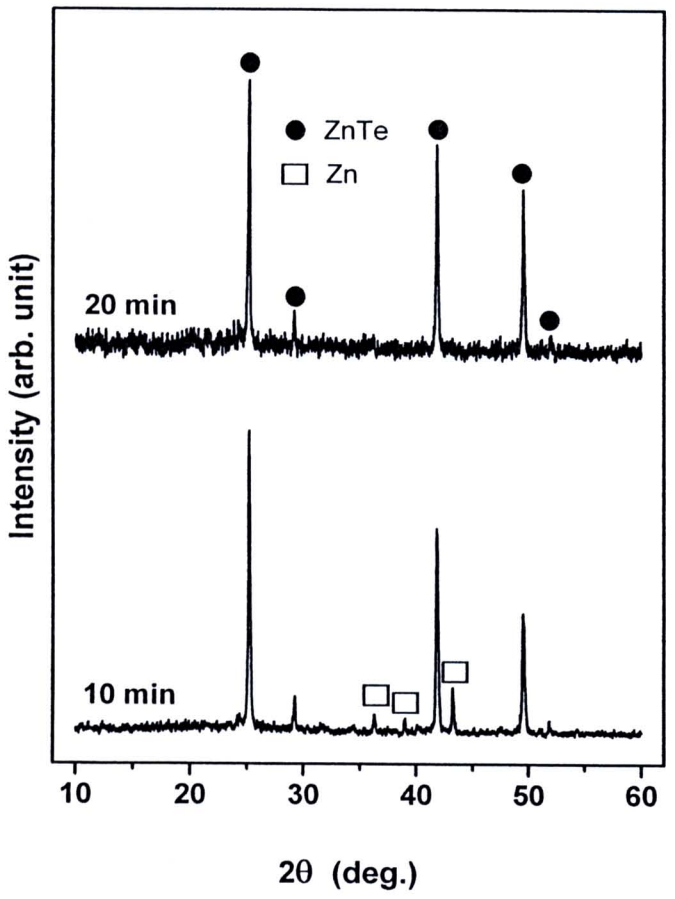

Figure 4.3 XRD spectra of the products prepared using 1.8:1 molar ratio of Zn:Te.

Table 4.3 Calculated lattice parameter of ZnTe from the experiment (molar ratio of Zn:Te = 1.8:1, 20 min.) comparing with the JCPDS file (Reference code: 15-0746).

Plane	2θ, Exp. (deg.)	2θ, JCPDS file (deg.)	Interplanar spacing (d), (Exp.) Å	Interplanar Spacing (d) JCPDS file, Å	Lattice parameter, (Exp.) Å	Lattice parameter, JCPDS file, Å
(111)	25.258	25.259	3.5218	3.5230	6.0999	6.1026
(200)	29.244	29.248	3.0502	3.0510	6.1004	6.1026
(220)	41.862	41.806	2.1554	2.1590	6.0964	6.1026
(311)	49.540	49.498	1.8378	1.8400	6.0954	6.1026
(222)	51.896	51.847	1.7598	1.7620	6.0961	6.1026
					6.0977±0.0023	

XRD patterns of the 1:1 molar ratio of Zn:Te and 40 min, 1.5:1 molar ratio of Zn:Te and 40 min, and 1.8:1 molar ratio of Zn:Te and 10 min products were also simulated using CaRIne Version 31 program [73] and $Cu\ K_\alpha$ line of 0.15406 nm. The results are shown in Figure 4.4. The 2θ diffraction angles and intensities (I) of different crystallographic planes obtained from the experiment, simulation, and the JCPDS database for cubic ZnTe [70] are summarized in Table 4.4 - 4.6. It is worth noting that these values are in good accordance: simulated patterns for particular conditions were created and used to specify the existence of the experimental patterns, which correspond very well with that of the JCPDS database [70].

Table 4.4 The 2θ diffraction angles and intensities of the JCPDS no. 15-0746 [70] for the 1:1 molar ratio of Zn:Te and 40 min product obtained from the experiment and simulation.

Plane	JCPDS		Experiment		Simulation	
	2θ (deg.)	Intensity (%)	2θ (deg.)	Intensity (%)	2θ (deg.)	Intensity (%)
(111)	25.259	100	25.236	100.00	25.27	100.0
(200)	29.248	10	29.230	14.19	29.26	6.7
(220)	41.806	80	41.868	87.18	41.85	63.7
(311)	49.498	35	49.528	52.71	49.52	38.2
(222)	51.847	4	51.850	4.89	51.88	1.4

Table 4.5 The 2θ diffraction angles and intensities of the JCPDS no. 15-0746 [70] for the 1.5:1 molar ratio of Zn:Te and 40 min product obtained from the experiment and simulation.

Plane	JCPDS		Experiment		Simulation	
	2θ (deg.)	Intensity (%)	2θ (deg.)	Intensity (%)	2θ (deg.)	Intensity (%)
(111)	25.259	100	25.240	100.00	25.27	100.0
(200)	29.248	10	29.240	16.16	29.26	6.7
(220)	41.806	80	41.856	78.36	41.85	63.7
(311)	49.498	35	49.514	43.02	49.52	38.2
(222)	51.847	4	51.908	5.15	51.88	1.4

Table 4.6 The 2θ diffraction angles and intensities of the JCPDS no. 15-0746 [70] for the 1.8:1 molar ratio of Zn:Te and 20 min product obtained from the experiment and simulation.

Plane	JCPDS		Experiment		Simulation	
	2θ (deg.)	Intensity (%)	2θ (deg.)	Intensity (%)	2θ (deg.)	Intensity (%)
(111)	25.259	100	25.258	100.00	25.28	100.0
(200)	29.248	10	29.244	17.96	29.27	6.7
(220)	41.806	80	41.862	77.07	41.87	63.7
(311)	49.498	35	49.540	61.00	49.54	38.2
(222)	51.847	4	51.896	8.15	51.90	1.4

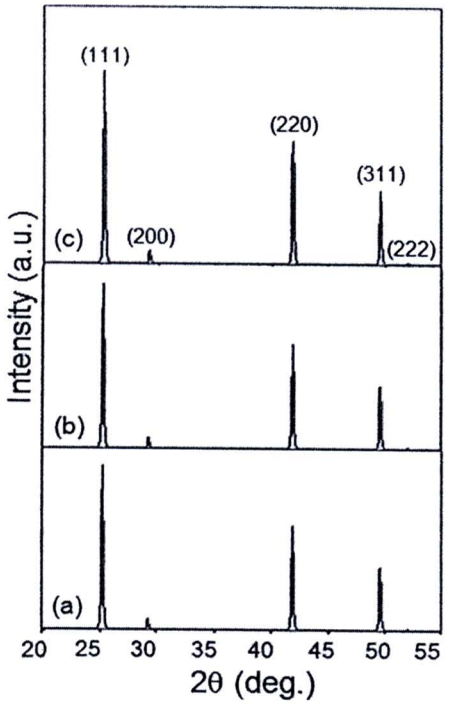

Figure 4.4 XRD spectra simulation of ZnTe at (a) 1:1, (b) 1.5:1 and (c) 1.8:1 molar ratio of Zn:Te.

Crystallite size (D) of ZnTe for 1:1 molar ratio and 40 min, 1.5:1 molar ratio and 40 min, and 1.8:1 molar ratio and 20 min products were calculated using the (111) peaks of the XRD spectra and the Scherrer's equation [71]

$$D = \frac{K\lambda}{\beta \cos\theta} \tag{4.1}$$

where K is the geometric (shaped) factor which usually takes a value of 0.9 [71,74], λ is the wavelength of $Cu\ K_\alpha$ radiation (0.15406 nm), and β and θ are the full width at half maximum and Bragg's angle of the (111) peak, respectively. The results of crystallite size (D) are shown in Table 4.7. The calculated crystallite size of ZnTe for the 1:1 molar ratio and 40 min, 1.5:1 molar ratio and 40 min, and 1.8:1 molar ratio and 20 min products are 77.52, 111.5, and 113.1 nm, respectively.

Table 4.7 The crystallite size (D) calculated from the Scherrer's equation and the full-width at half maximum (FWHM) of the XRD spectra.

Experiment	2θ	θ	β	D (Å)	D (nm)
1:1 molar ratio of Zn:Te, 40 min	25.236	12.618	0.105	775.2	77.52
1.5:1 molar ratio of Zn:Te, 40 min	25.240	12.620	0.073	1115	111.5
1.8:1 molar ratio of Zn:Te,20 min	25.258	12.629	0.072	1131	113.1

Figure 4.5 shows Raman spectra of cubic ZnTe nanocrystals, which were composed of three longitudinal optical (LO) modes of 1LO (1st harmonic or fundamental), 2LO (2nd harmonic or 1st overtone) and 3LO (3rd harmonic or 2nd overtone) at 205, 410, and 620 cm^{-1}, and one transverse optical (TO) mode at 166 cm^{-1}, respectively. These Raman shifts are in good accordance with those obtained by Jiang et al. [51], who specified the 1LO, 2LO and TO Raman shifts of ZnTe nanowires at 198, 396 and 168 cm^{-1}, respectively. Comparing to 30 mW He-Ne laser with 632.8 nm (red) wavelength, a great deal of energy was lost during the Raman analysis, due to the inelastic scattering process.

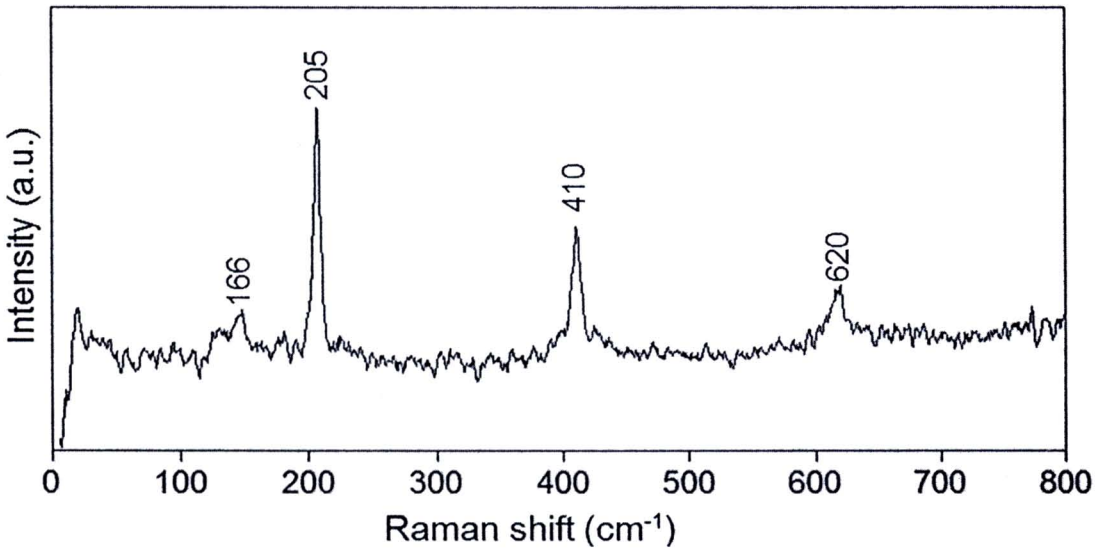

Figure 4.5 Raman spectra of ZnTe synthesized using 1:1 molar ratio of Zn:Te for 40 min.

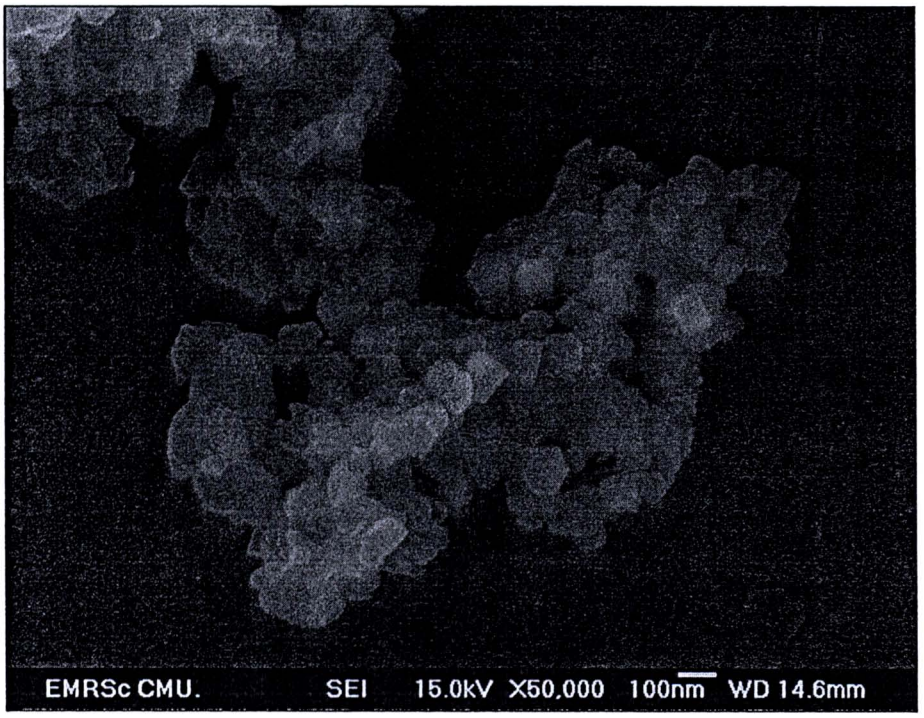

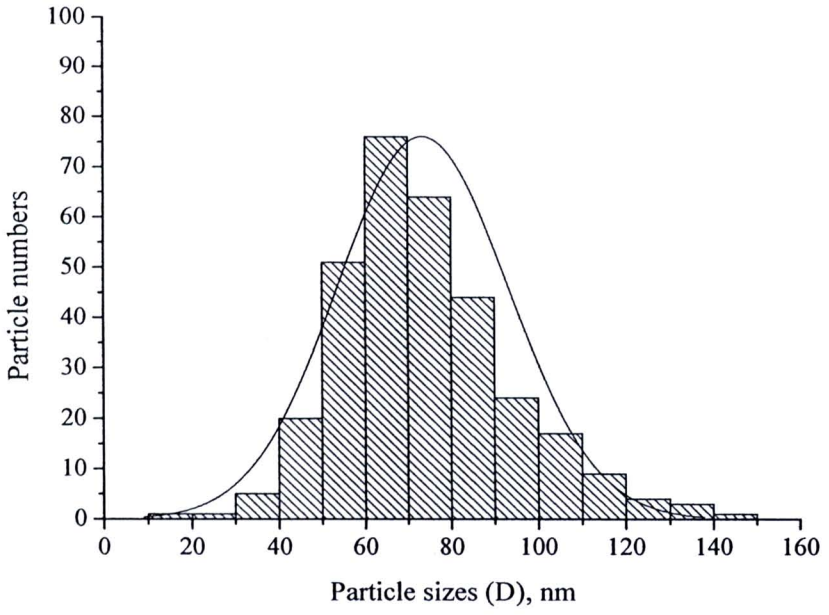

Figure 4.6 SEM image and particle size distribution of ZnTe produced under the 1:1 molar ratio of Zn:Te for 40 min condition.

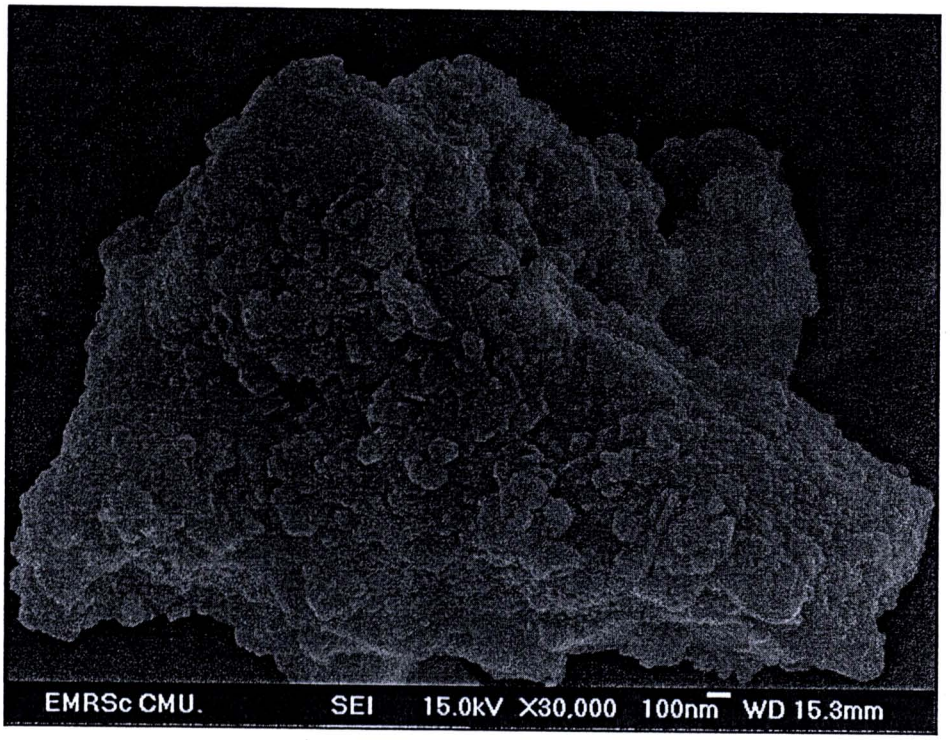

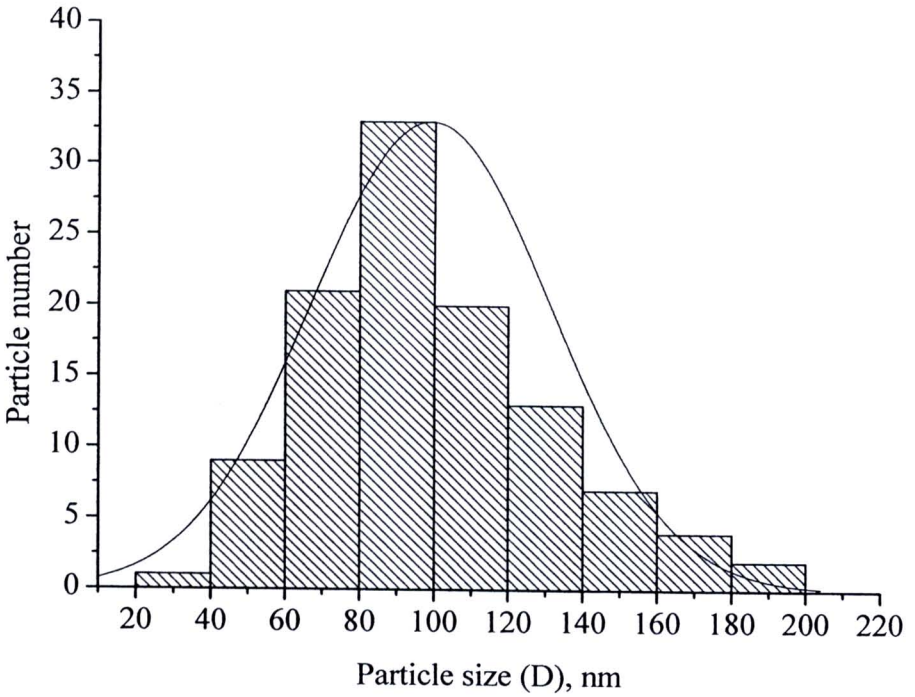

Figure 4.7 SEM image and particle size distribution of ZnTe produced under the 1.5:1 molar ratio of Zn:Te for 40 min condition.

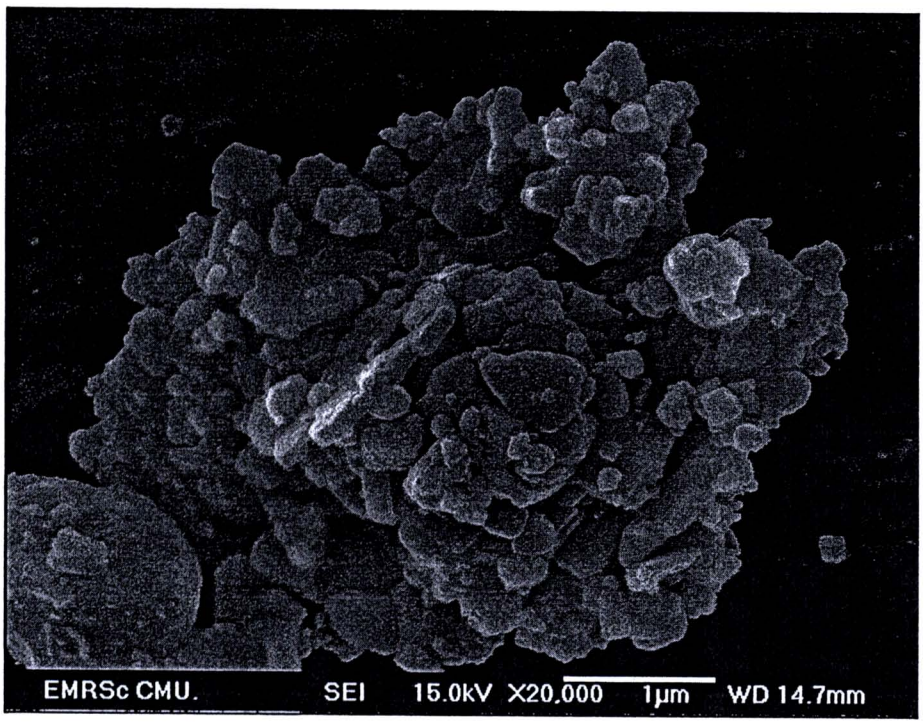

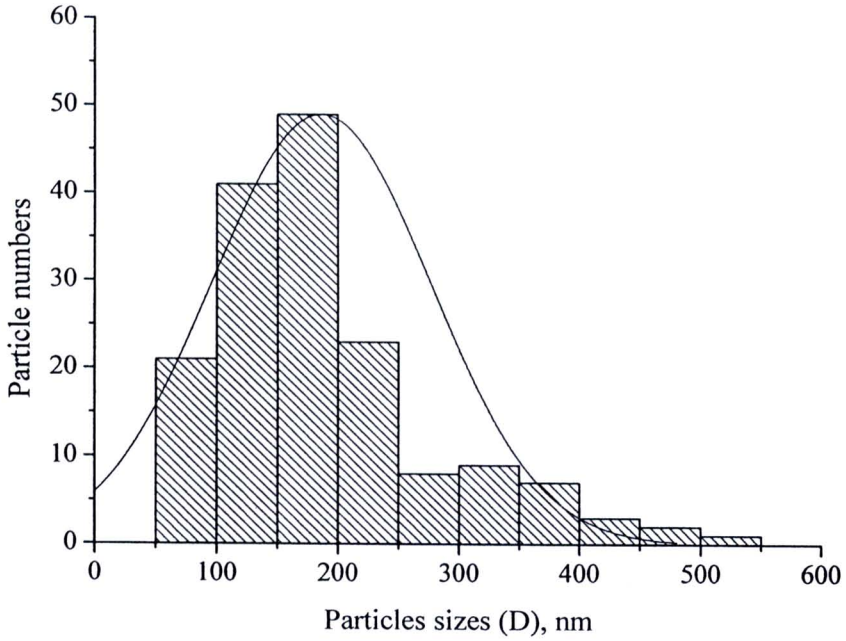

Figure 4.8 SEM image and particle size distribution of ZnTe produced under the 1.8:1 molar ratio of Zn:Te for 20 min condition.

SEM image and particle size distribution of the powder (Figure 4.6) showed that morphologies of the products prepared at 1:1 molar ratio of Zn:Te for 40 min, are individually round particles with the size of nanometer. The product was composed of rather round 73.37± 19.81 nm nanoparticles with some facets and different orientations. This average size is in accordance very well with that calculated using the Scherrer's equation. But for ZnTe at 40 min of 1.5:1 and 20 min of 1.8:1 molar ratio of Zn:Te product, it is composed of a number of nanoparticles in irregular clusters as shown in Figures 4.7 and 4.8. The average size of ZnTe at 1.5:1 and 1.8:1 molar ratios of Zn:Te are 98.99 ± 32.28 and 186.33 ± 90.50 nm, respectively. The values of average sizes were different from those calculated using the Scherrer's equation, because both conditions produced different sizes of clusters and average sizes of particles are measured on the surface of clusters. The nanoparticles of ZnTe at 1.5:1 molar ratio of Zn:Te condition forming as clusters have small-size than at 1.8:1 molar ratio of Zn:Te. Therefore the calculated crystallite size of particle from Scherrer's equation using full width at half maximum is the average values of total particles. The average size of SEM image was obtained from only the selected area on surface of the clusters, and did not cover the total particles.

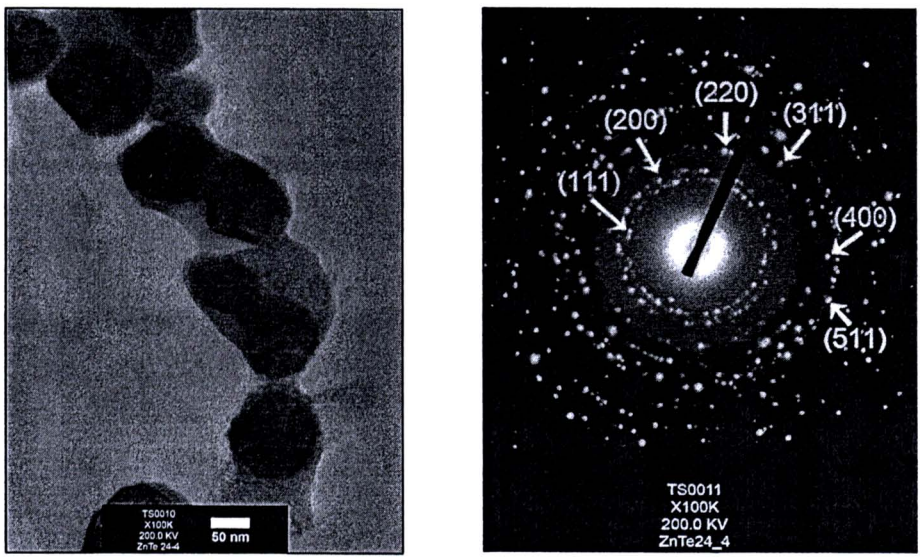

(a) (b)

Figure 4.9 TEM image (a), and SAED pattern (b) of ZnTe produced under the 1:1 molar ratio of Zn:Te condition.

Table 4.8 Ring diffraction pattern values of ZnTe produced under the 1:1 molar ratio of Zn:Te condition, and the parameters of the JCPDS standard.

Ring No.	Diameter (mm)	Radius, R, (mm)	$d = L\lambda/R$ (°A) (calculated)	d (°A) (JCPDS file No.15-0746)	(hkl)
1	14.2	7.10	3.51592	3.523	111
2	16.7	8.35	2.98958	3.051	200
3	23.7	11.85	2.10658	2.159	220
4	27.7	13.85	1.80238	1.840	311
5	33.2	16.60	1.50380	1.526	400
6	43.2	21.60	1.15569	1.1745	511

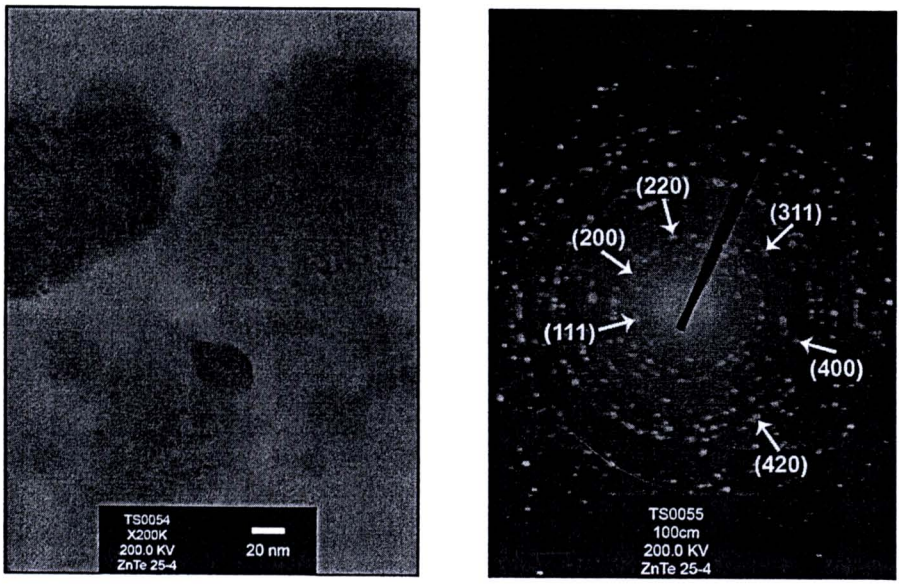

(a) (b)

Figure 4.10 TEM image (a) and SAED pattern (b) of ZnTe produced under the 1.5:1 molar ratio of Zn:Te condition.

Table 4.9 Ring diffraction pattern values of ZnTe produced under the 1.5:1 molar ratio of Zn:Te condition, and the parameters of the JCPDS standard.

Ring No.	Diameter (mm)	Radius, R, (mm)	$d = L\lambda/R$ (°A) (calculated)	d (°A) (JCPDS file No.15-0746)	(hkl)
1	14.0	7.00	3.56614	3.523	111
2	17.0	8.50	2.93682	3.051	200
3	22.0	11.00	2.26936	2.159	220
4	26.0	13.00	1.92023	1.840	311
5	32.0	16.00	1.56019	1.526	400
6	36.0	18.00	1.38683	1.3645	420

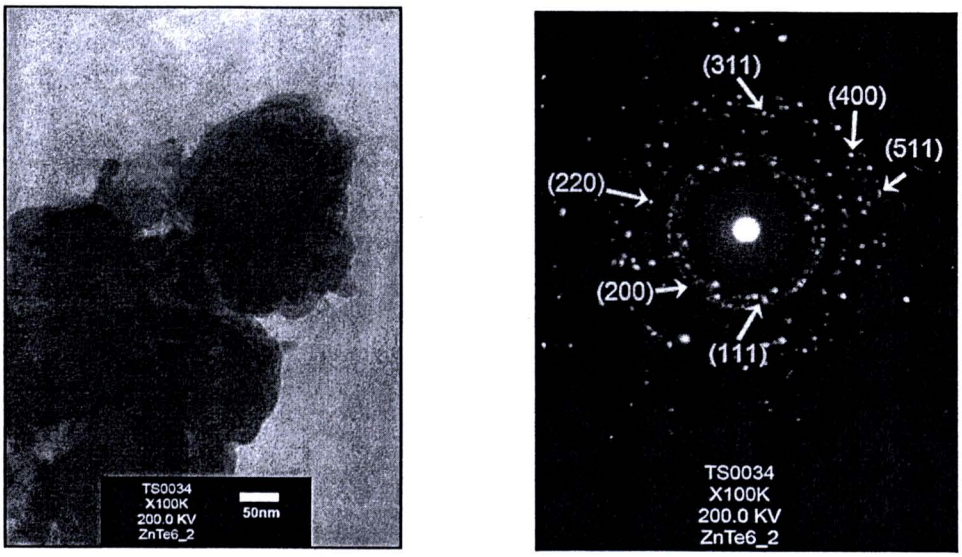

(a) (b)

Figure 4.11 TEM image (a) and SAED pattern (b) of ZnTe produced under the 1.8:1 molar ratio of Zn:Te condition.

Table 4.10 Ring diffraction pattern values of ZnTe produced under the 1.8:1 molar ratio of Zn:Te condition, and the parameters of the JCPDS standard.

Ring No.	Diameter (mm)	Radius, R, (mm)	$d = L\lambda/R$ (°A) (calculated)	d (°A) (JCPDS file No.15-0746)	(hkl)
1	14.7	7.35	3.39633	3.523	111
2	16.7	8.35	2.98958	3.051	200
3	22.7	13.85	2.19938	2.159	220
4	27.7	15.35	1.80238	1.840	311
5	32.7	16.35	1.52679	1.526	400
6	43.5	21.75	1.14772	1.1745	511

TEM images and SAED patterns of the products prepared by the microwave plasma are shown in Figures 4.9 – 4.11. The ZnTe powder prepared at 1:1 molar ratio of Zn:Te was composed of rather round 70 – 80 nm nanoparticles, which is in accordance very well with those calculated using the Scherrer's equation and SEM image. The products at 1.5:1 and 1.8:1 molar ratio of ZnTe conditions clustered together in groups, due to the rapid reaction proceeding by the increase of Zn in the reaction. TEM and SEM analyses are in good accordance. The SAED patterns (Figures 4.9b – 4.11b) of the 1:1, 1.5:1 and 1.8:1 molar ratios of ZnTe products appeared as concentric rings of bright spots, showing that these products were composed of a number of nanocrystals with different orientations. The interplanar spacings were calculated using diameters of the diffraction rings [75], and compared with those of the JCPDS standard [70]. The rings corresponded to the (111), (200), (220), (311), (400) and (511) planes of cubic ZnTe, produced under both the 1:1 and 1.8:1 molar ratios of ZnTe conditions. For 1.5:1 molar ratio of ZnTe condition, the rings correspond to the (111), (200), (220), (311), (400) and (420) planes.

Photoluminescence (PL) properties of cubic ZnTe were studied at room temperature, using 370 nm excitation wavelength from a xenon laser. Their spectra (Figures 4.12-4.14) were green emission centered at 562 nm (2.21 eV), possibly associated with point defects located at 0.4 eV above the valence band edge [6]. The emission were in accordance with those detected by Jiang et al (560 nm or 2.21 eV emitted from ZnTe nanowires) [51], and Park et al (552 nm (2.25 eV) emitted from 14 nm nanocrystals) [76]. Comparing to ZnTe (bulk) with 2.26 eV band gap, the present emission has a slight red shift, which could be influenced by the twins in nanowires [51].

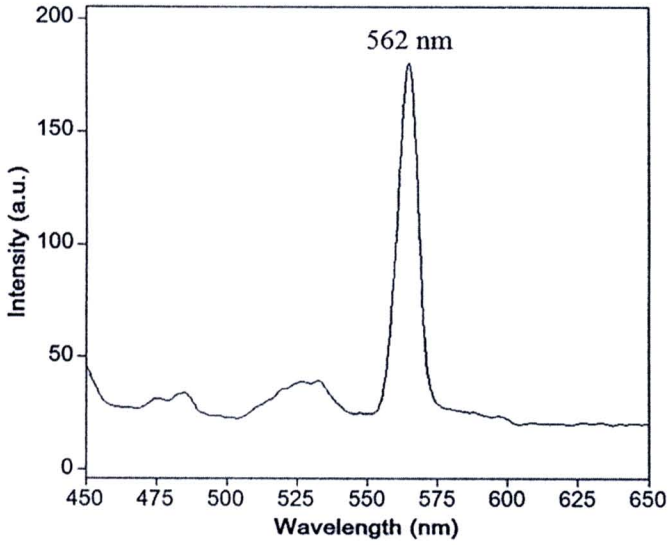

Figure 4.12 Photoluminescence of ZnTe produced under the 1:1 molar ratio of Zn:Te condition.

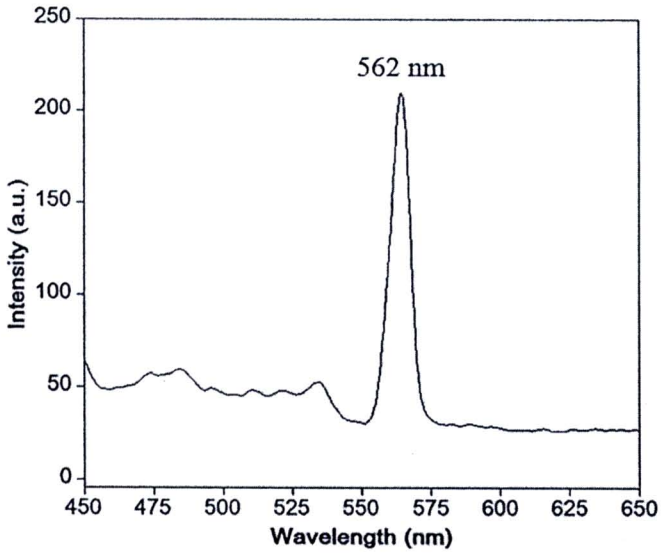

Figure 4.13 Photoluminescence of ZnTe produced under the 1.5:1 molar ratio of Zn:Te condition.

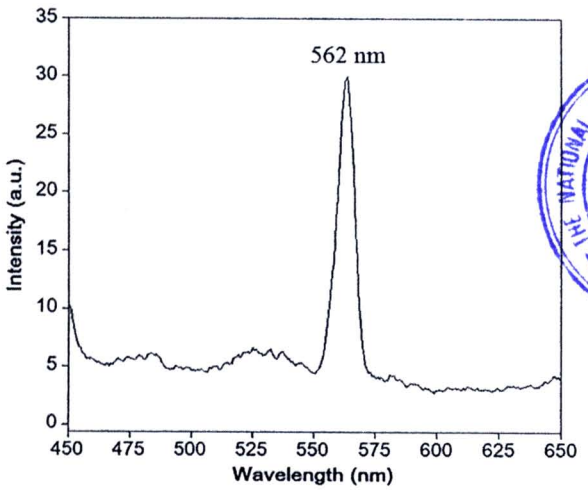

THE NATIONAL RESEARCH COUNCIL OF THAILAND
RESEARCH LIBRARY

Figure 4.14 Photoluminescence of ZnTe produced under the 1.8:1 molar ratio of Zn:Te condition.

Comparing the emission of the 1:1, 1.5:1 and 1.8:1 molar ratios of Zn:Te products, the intensities became stronger in sequence as follows: 1.5:1, 1.1:1 and 1.8:1 molar ratios of Zn:Te, respectively, although intensity of the 1.5:1 molar ratio of Zn:Te product was almost the same as that of the 1:1 molar ratio of Zn:Te product. Among these three products, the 1.5:1 molar ratio Zn:Te atoms were arranged in higher order than the 1:1 and 1.8:1 molar ratios of Zn:Te atoms, resulting from the difference in the reaction times and molar ratio of Zn:Te, the 1.5:1 and 1:1 molar ratios of Zn:Te conditions took longer than the 1.8:1 molar ratio of Zn:Te condition. Rate of reaction depend on concentration of reactants [72], therefore increasing of Zn has affected to increase the driving force of reaction, which promotes the reaction rate to become faster. For high reaction rate, atoms were arranged in the crystalline structure with low crystalline degree, which promoted the formation of some imperfections such as dislocations and other defects.

4.2 Sb_2Te_3 by microwave plasma

XRD spectra (Figure 4.15) of the products synthesized using different molar ratios of Sb:Te at 900 W microwave plasma for different lengths of time were compared with the JCPDS database [70]. At a 2:3 molar ratio of Sb:Te, for 10 and 20 min, the products were Sb_2Te_3 (JCPDS no. 15-0874) containing some Te residue (JCPDS no. 36-1452). This residue still remained in the product, although the lengths of time were as long as 40 min. The amount of Te was reduced in a series of steps until at 2:2, 2:1.75, and 2:1.5 molar ratios of Sb:Te, with lengths of time of 10 and 20 min – the products were Sb_2Te_3, without any residual detection. At these stages, Sb and Te completely combined together chemically to form Sb_2Te_3 with a rhombohedral crystal system and R-3m space group [70]. During microwave plasma heating, some of the Sb and Te could evaporate as well.

In the present research, approximate crystallite sizes (D) of Sb_2Te_3 crystals synthesized under different conditions were calculated using the Scherrer formula (Equation 4.1); Bragg angles of the (015) peaks; a constant (0.90); and full widths at half maximum of the peaks. Calculated crystallite sizes of Sb_2Te_3 crystals synthesized by the 900 W microwave plasma at different molar ratios of Sb:Te and lengths of time are shown in Table 4.11. The crystallite sizes increased by 28–43 % by increasing the lengths of time from 10 min to 20 min with the microwave power remaining at 900 W; sizes increased by 27 % and 36 % by changing the Sb:Te molar ratios from 2:1.50 to 2:2 with the lengths of time remaining at 10 min, and 20 min, respectively. These results implied that the molar ratios and lengths of reaction time played key roles in the phase and crystallite sizes of Sb_2Te_3 crystals.

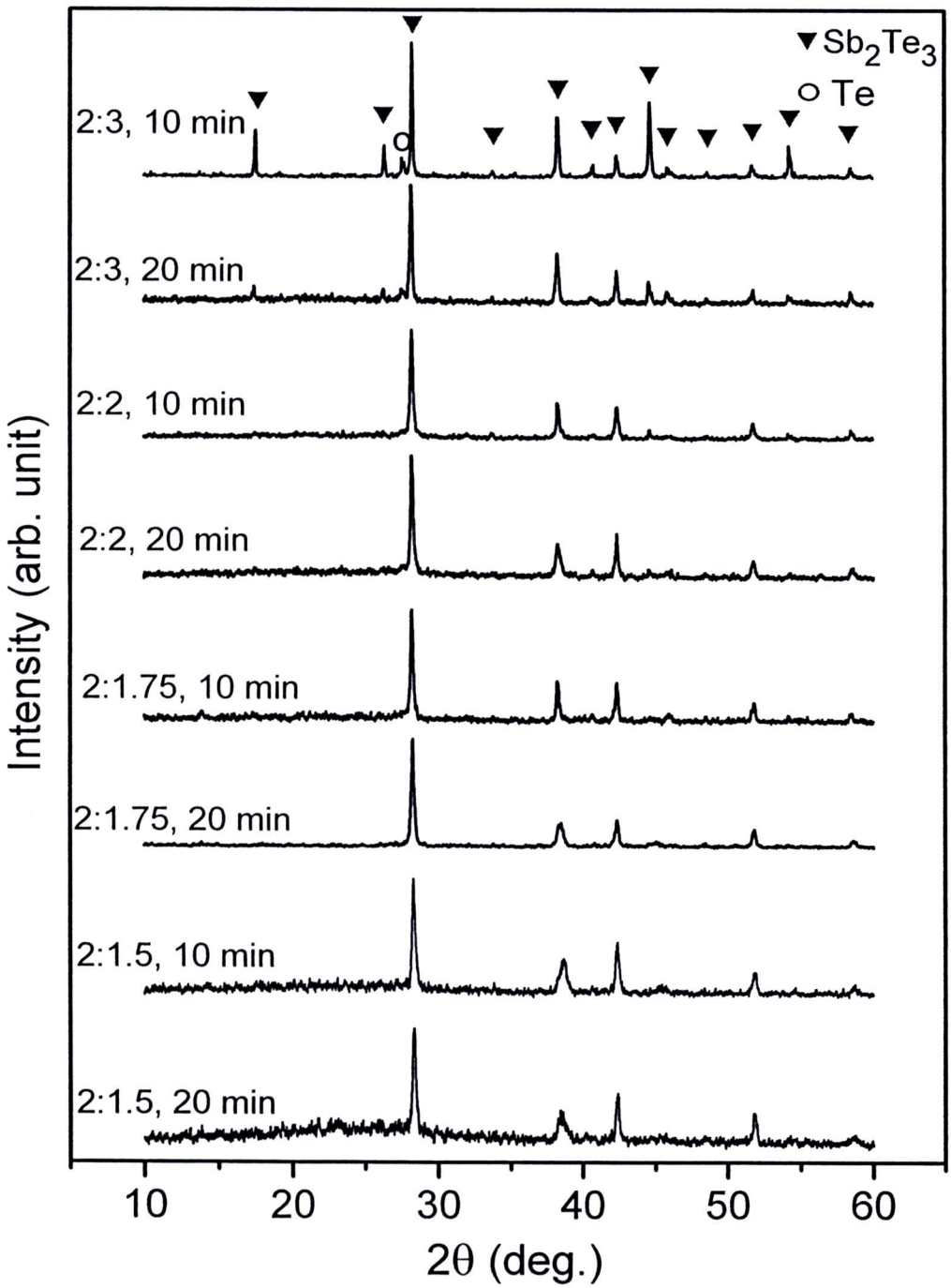

Figure 4.15 XRD spectra of the products synthesized using 900 W microwave plasma at different molar ratios of Sb:Te for 10 min and 20 min.

Table 4.11 Crystallite sizes of Sb_2Te_3 crystals synthesized at different Sb:Te molar ratios and lengths of time by 900 W microwave plasma.

Sb:Te (molar ratio)	Length of time (min)	Crystallite size (nm)
2:1.50	10	85.8
2:1.50	20	110.0
2:1.75	10	88.8
2:1.75	20	127.3
2:2	10	109.2
2:2	20	150.1

To further ascertain the presence of Sb_2Te_3, the products were characterized using Raman spectroscopy. Figure 4.16 shows four Raman shifts of Sb_2Te_3 crystals at 93.9, 102.6, 139.2 and 263.7 cm^{-1}. These peaks are in good accordance with those of pure Sb_2Te_3 characterized by Zheng et al. [62]. Compared to a 30 mW He-Ne laser with 632.8 nm (red) wavelength, a great deal of energy was lost during Raman analysis, caused by the inelastic scattering process.

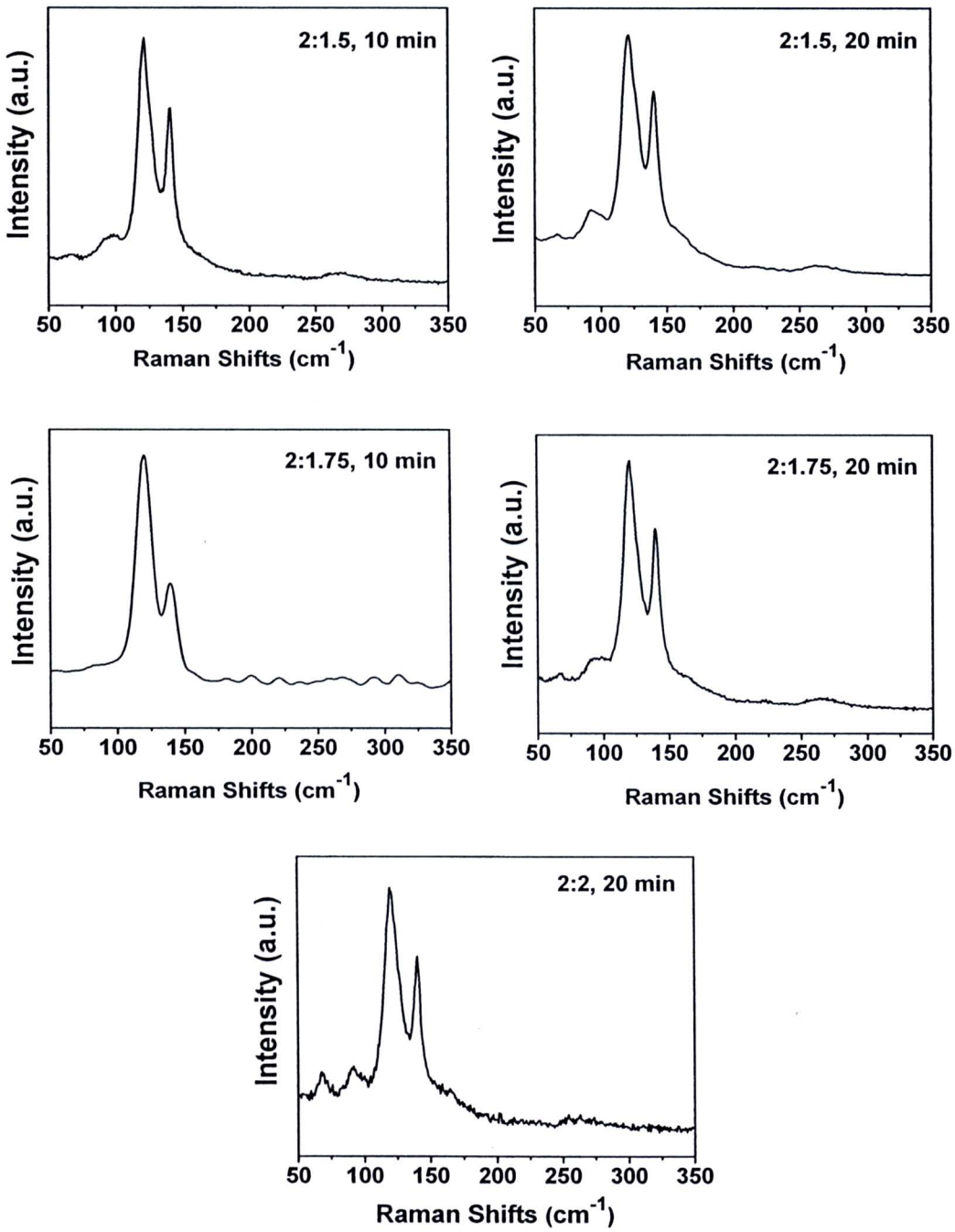

Figure 4.16 Raman spectra of Sb_2Te_3 synthesized using 900 W microwave plasma for different molar ratios of Sb:Te and lengths of time

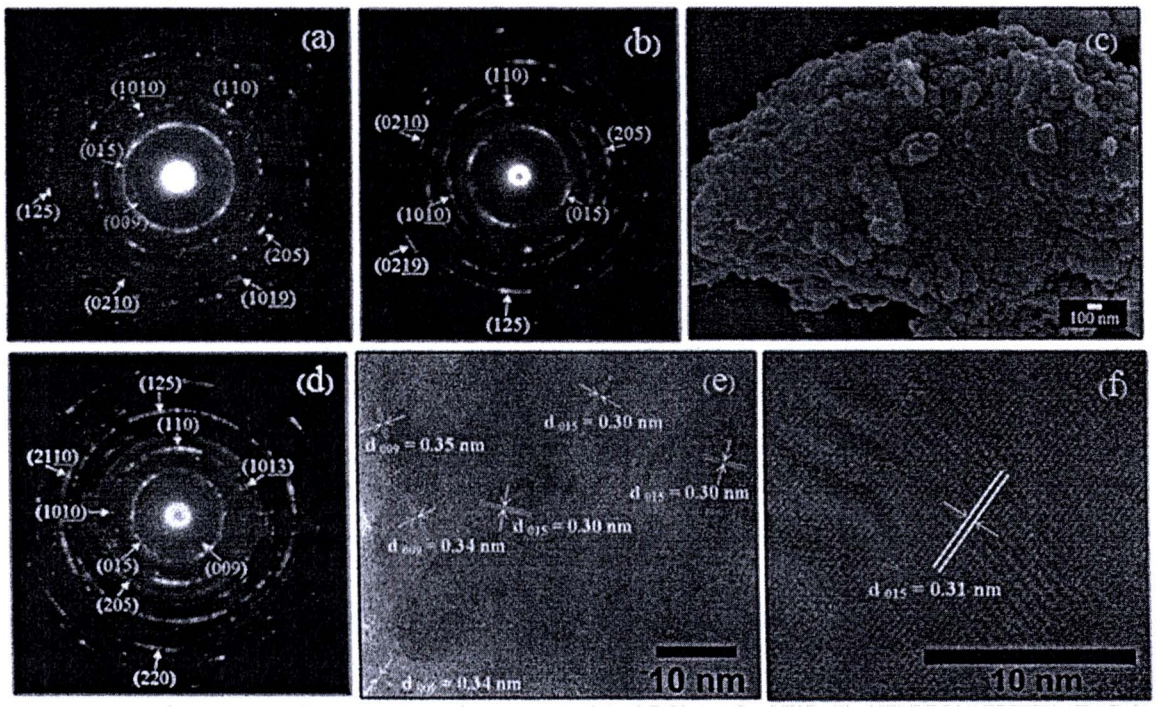

Figure 4.17 SAED patterns, and SEM and HRTEM images of Sb_2Te_3 synthesized using 900 W microwave plasma for different molar ratios of Sb:Te and lengths of time. (a) 2:1.5, 10 min; (b, c) 2:1.5, 20 min; and (d - f) 2:2, 20 min.

SAED patterns (Figure 4.17a, b and d) of the products, synthesized under different conditions, are composed of several concentric rings of diffuse spots caused by the diffraction of transmitted electrons through a number of crystals with different orientations. These interpreted patterns [75] were in accordance with a rhombohedral Sb_2Te_3 crystal system [70]. Its concentration could be too low to be detected by the analysis. A typical example of a SEM image of Sb_2Te_3, produced from a 2:1.5 molar ratio of Sb:Te for 20 min, is shown in Figure 4.17c. This product was composed of a number of nanocrystals with different orientations. A number of crystallographic planes with different orientations of different products (Figure 4.17e and f) were also

detected by high-resolution TEM (HRTEM). Their spaces correspond to those of the JCPDS database for a rhombohedral Sb_2Te_3 crystal system [70], showing the presence of crystals with different orientations composing the polycrystalline products. Compared with synthesis by other methods, there are some differences in Sb_2Te_3 products: hexagonal nanoplates by hydrothermal/solvothermal reactions [58,59], microwave-assisted synthesis [60], and aerosol-assisted chemical vapor deposition [63]; nanobelts by a hydrothermal process [61]; nanowire arrays using a porous anodic alumina membrane as a template by electrochemical deposition [64]; single-crystal nanowires by vapor-liquid-solid method [77]; films produced in a dense plasma focused device [65], and by thermal evaporation [66]; and nanostructures (nanowires, nanobelts and nanotubes) by the vapor-transport method [67]. These analyses prove that synthesis methods, starting reagents, pH values, templates, and other factors can play roles in product morphologies.

Figure 4.18 shows the $(\alpha_{abs}hv)^2$ and (hv) plots (Equation 3.1-3.3) for the direct allowed transition, where α_{abs}, h and v are respectively the total absorption coefficient, Planck constant, and photon frequency [69,78-79]. The direct energy band gaps were determined by extrapolating the linear parts of these curves to $\alpha_{abs} = 0$, at which the absorption went to zero with a range of 0.340–0.515 eV (as shown in Figure 4.18 and Table 4.12). These direct band gaps are in accordance with those in the 0.29–0.46 eV range for Sb_2Te_3 nanofilms with a thickness between 61.2 nm (35 min deposition) and 4.1 nm (10 min deposition) as determined by Erdoğan and Demir [80], and 0.42 eV for the 400-cycle Sb_2Te_3 film (190 nm thick) as determined by Yang et al. [81]. In the case of the last product (2:2 molar ratio of Sb:Te for 20 min), the E_g was reduced to be 0.340 eV. Possibly, undetectable impurities/residues existed in the product. These

direct band gaps are the fundamental parameters used to control the optoelectronic and thermoelectric properties of Sb_2Te_3 crystals. In general, the energy band gap was influenced by the processing syntheses, morphologies, average crystallite sizes, and degrees of structural order-disorder. Some defects could form in the crystalline lattice during synthesis. This promoted the presence of intermediate levels between the valence and conduction bands, which can play the role in the band gap of the products, as well as in their optoelectronic and thermoelectric properties.

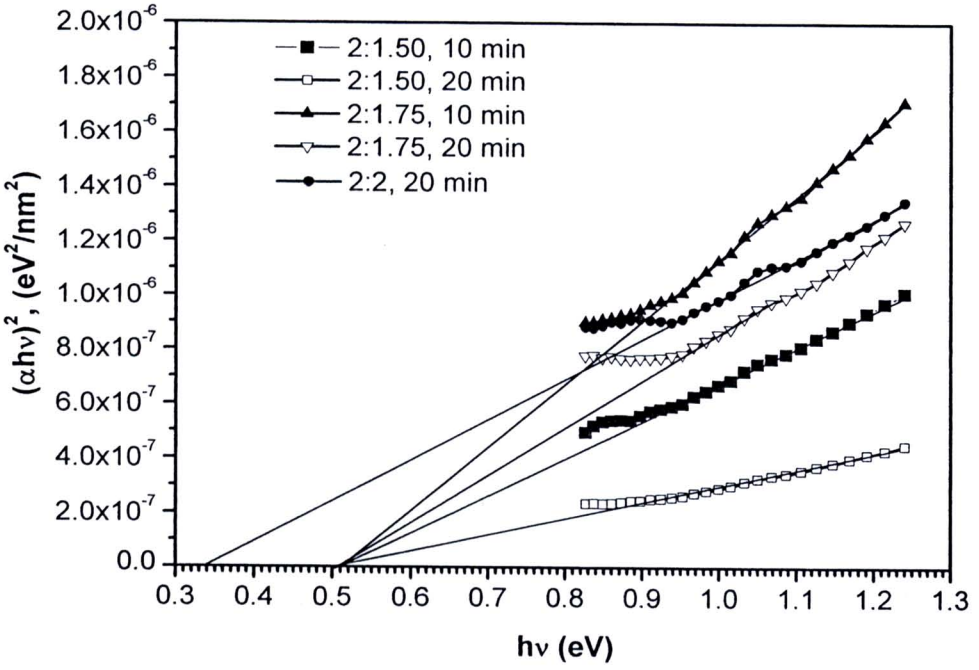

Figure 4.18 The $(\alpha_{abs}hv)^2$ vs (hv) plots of Sb_2Te_3, synthesized at different Sb:Te molar ratios and lengths of time by a 900 W microwave plasma.

Table 4.12 Direct energy band gaps of Sb_2Te_3 crystals synthesized at different Sb:Te molar ratios and lengths of time by a 900 W microwave plasma.

Sb:Te (molar ratio)	Length of time (min)	Crystallite size (nm)	E_g (eV)
2:1.50	10	85.8	0.515
2:1.50	20	110.0	0.515
2:1.75	10	88.8	0.515
2:1.75	20	127.3	0.515
2:2	10	109.2	-
2:2	20	150.1	0.340

4.3 Ni_3GaSb and Ni_3InSb by alloying preparation in a furnace

The powder XRD patterns of the prepared samples are shown in Figure 4.19. Both the samples were identified as Ni_3GaSb and Ni_3InSb, according to the JCPDS database (Reference codes: 47-1401 for Ni_3GaSb, and 47-1402 for Ni_3InSb) [68,70], although these compounds contained a few peaks that were inconsistent with the JCPDS data. Therefore, the XRD experimental data were analyzed by the Rietveld refinement [82] on the X-ray diffraction patterns, using the hexagonal crystal system with the space group of P63/mmc. Details of the structure are reported in Ref. 68. Refinement of the patterns for both compounds revealed that all the reflections were indexed to be Ni_3GaSb and Ni_3InSb phases, with no evidence of the impurities as shown in Figure 4.20. Two peaks of the (100) and (203) planes of Ni_3GaSb and

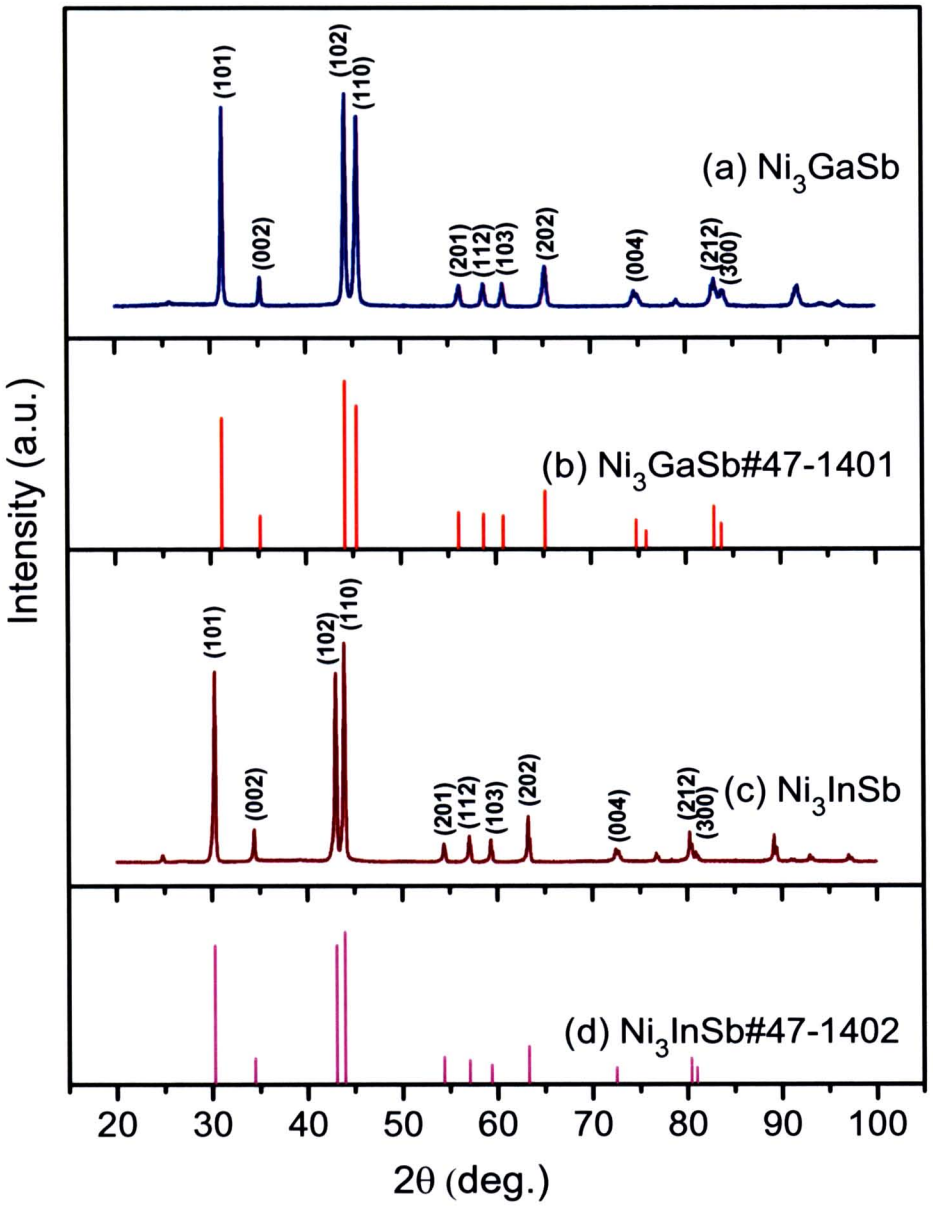

igure 4.19 Powder XRD patterns of the polycrystalline samples; (a) Ni_3GaSb and (b) Ni_3InSb, including their databases (c) and (d) [68].

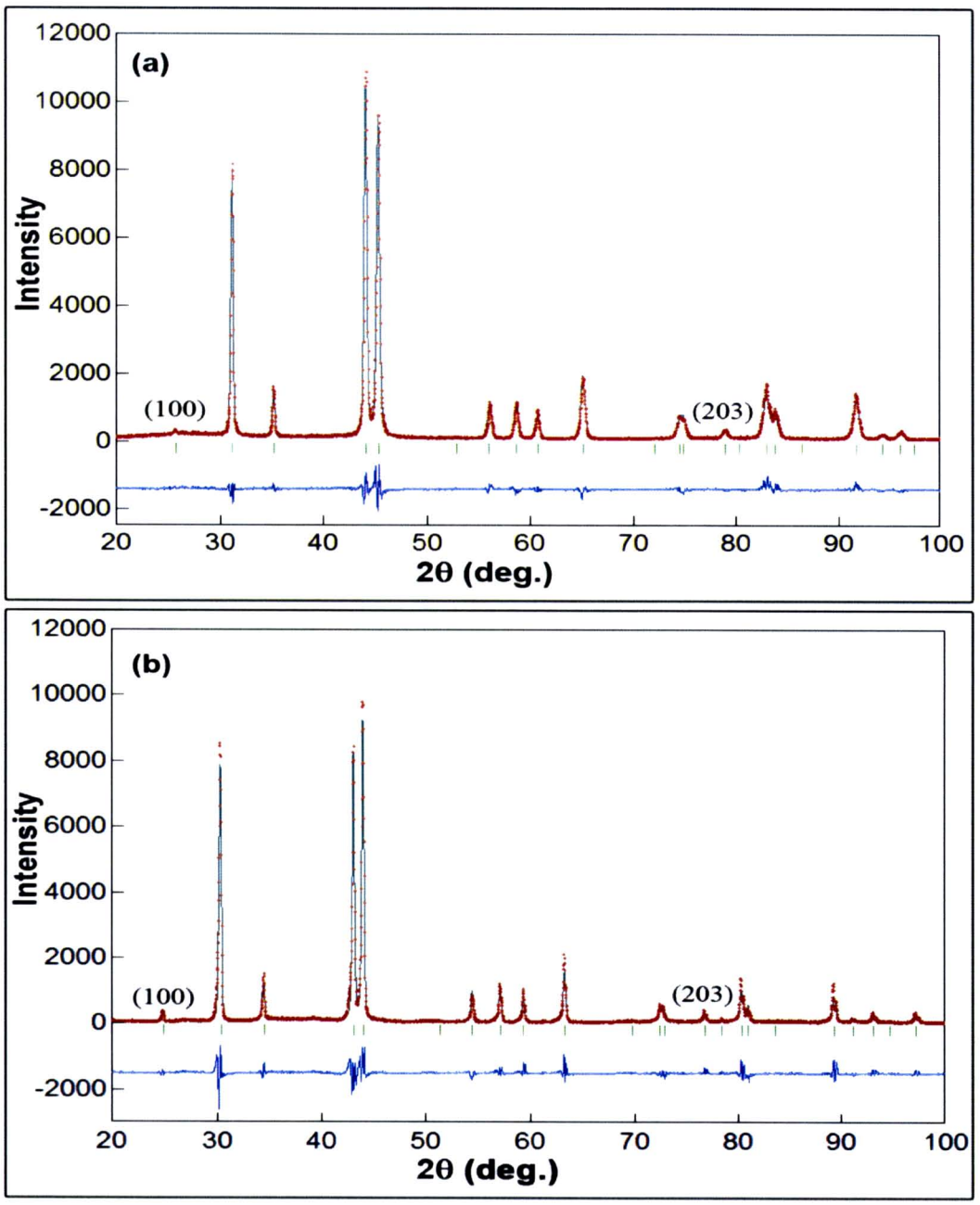

gure 4.20Powder XRD patterns of the polycrystalline samples and the results of the ietveldrefinement of (a) Ni_3GaSb and (b) Ni_3InSb. The experimental data are labelled as nall red crosses, the calculated fits and the difference curves are shown as blue solid lines. nort vertical lines (green) below the patterns indicate the calculated peak positions.

The crystal structures of the compounds are shown in Figure 4.21. According to ecrystal structure of Ni_3GaAs [83], Ni atoms occupythe (0,0,0) and the (0,0,1/2) positions;

ne vacancy and one Ni atomrandomlyoccupy the (2/3,1/3,1/4) and the (1/3,2/3,3/4) ositions; andGa and As atoms randomlyoccupy the (1/3,2/3.1/4) and the (2/3,1/3,3/4) ositions. The results of the Rietveld analysis for Ni_3GaSb and Ni_3InSb were in good greement with the structure of Ni_3GaAs.

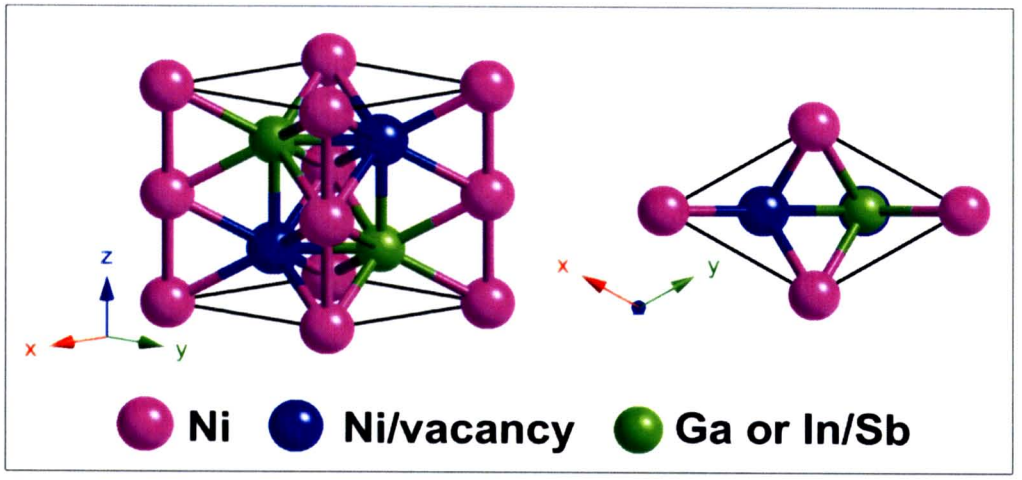

Figure 4.21 Crystal structures of Ni_3GaSb and Ni_3InSb.

The lattice parameters, sample bulk density, and chemical composition of the samples e summarized in Table 4.13. The hexagonal lattice parameters and the theoretical density of ese compounds were in good agreement with those reported by Jan and Chang [68]. The ensities of the polycrystalline samples obtained from the sintered specimens for TE haracterizations were 96% of the theoretical density. All the samples appeared to be stable air at room temperature. The quantitative EDX analysis confirmed that the chemical mpositions of the bulk sintered samples corresponded to theirstoichiometric mpositions,summarized in Table4.13.

analysis confirmed that the chemical compositions of the bulk sintered samples corresponded to their stoichiometric compositions, summarized in Table 4.13.

Table 4.13 Lattice parameters, sample bulk density, and chemical composition of Ni_3GaSb and Ni_3InSb.

		Ni_3GaSb	Ni_3InSb
Lattice parameter	$a = b$ (Å)	4.0135 [4.0000]	4.1111 [4.1100]
	c (Å)	5.1136 [5.0900]	5.1882 [5.1900]
Theoretical density	d_{th} (gcm^{-3})	8.56 [8.65]	8.97 [9.03]
Measured density	d_{exp} (gcm^{-3})	8.18	8.60
Relative density	$d_{exp/dth} \times 100$ (%)	96	96
Chemical composition determined through the EDX analysis (at.%)	Ni	59.5	59.9
	Ga	20.1	-
	In	-	20.0
	Sb	20.4	20.1

[ ] : Ref 68

The SEM and EDX mapping images of the bulk Ni_3GaSb and Ni_3InSb samples are shown in Figure 4.22. The SEM images indicated that both samples were homogeneous. The EDX analysis revealed that Ni, Ga, In, and Sb were uniformly distributed on the sample surfaces. The SEM and EDX analyses confirmed that the Ni_3GaSb and the Ni_3InSb samples were homogeneous with their stoichiometric chemical compositions, corresponding to their chemical formulas.

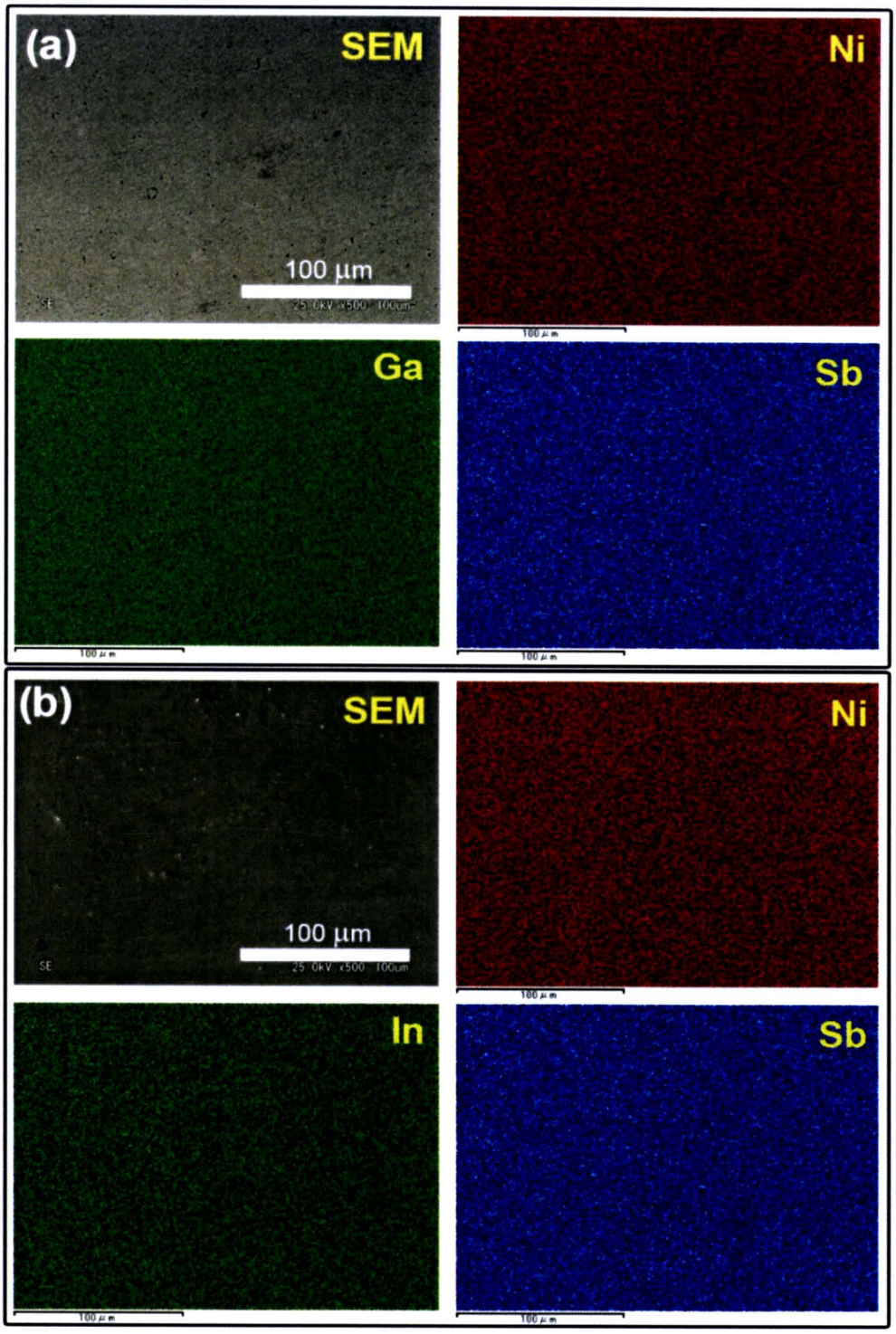

gure4.22 SEM and EDX mapping images of the (a) Ni_3GaSb and (b) Ni_3InSb bulk samples.

The temperature dependence of the electrical properties of the Ni_3GaSb and the Ni_3InSb samples is shown in Figure 4.23. The electrical resistivity (ρ) of both samples exhibited a metal-like behavior; increased with temperature in the whole temperature range and reached a maximum at 1073 K, as shown in Figure 4.23(a). The Seebeck coefficient (α) values were negative for both samples, as shown in Figure 4.23(b), indicating that the majority of charge carriers was electrons. The absolute α values of these samples increased with temperature and were constant at around 900 to 1073 K. The absolute α values were quite low like metals; the α values of Ni_3GaSb and Ni_3InSb at 1073 K were -21 and -22 μVK^{-1}, respectively. Ni_3GaSb exhibited the lower ρ and the absolute α values than those of Ni_3InSb, most likely due to the larger carrier concentration of Ni_3GaSb than that of Ni_3InSb as the data summarized in Table 4.14. The power factor ($\alpha^2\rho^{-1}$) data of the samples were plotted as a function of temperature in Figure 4.23(c). The power factor was increased with temperature and was constant at around 900 to 1073 K. The maximum values of the power factor of Ni_3GaSb and Ni_3InSb were achieved at 1073 K to be 0.43 and 0.45 $mWm^{-1}K^{-2}$, respectively. These values were larger than those of the related compounds such as pure GaSb (8.82 $\mu Wm^{-1}K^{-2}$, 322K) [92], and InSb (35 $\mu Wm^{-1}K^{-2}$, 350K) [93].

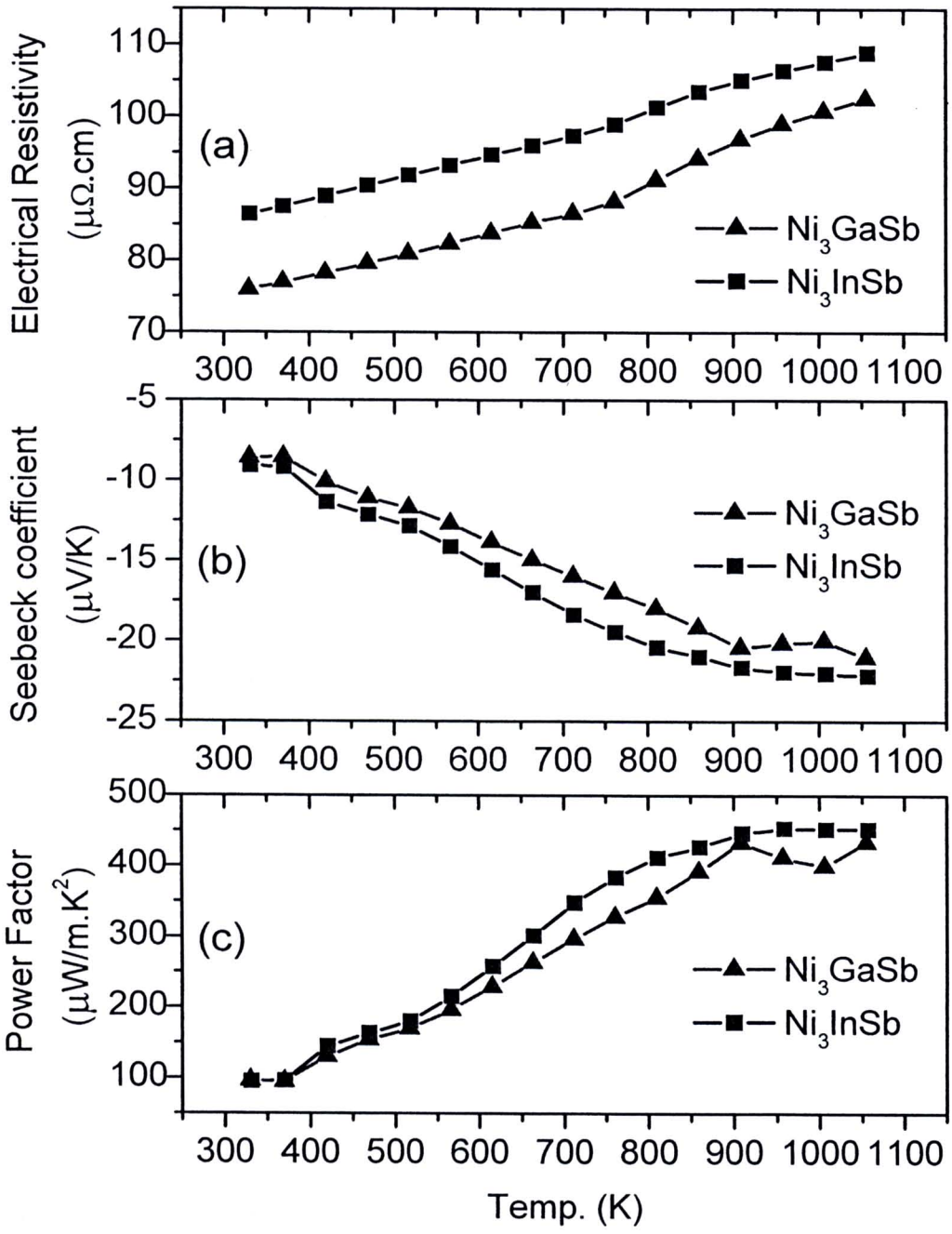

Figure 4.23 Temperature dependence of the electrical properties of Ni_3GaSb and Ni_3InSb polycrystalline samples: (a) electrical resistivity ρ, (b) Seebeck coefficient α, and (c) power factor $\alpha^2\rho^{-1}$.

Table 4.14 Hall coefficient (R_H), Hall carrier concentration (n_H), and Hall Mobility (μ_H) at 300 K

Compounds	R_H (10^{-5}cm^3 C^{-1})	n_H (10^{22}cm^{-3})	μ_H (cm^{2}V^{-1}s^{-1})
Ni_3GaSb	8.65	7.21	1.27
Ni_3InSb	39.8	1.57	5.01

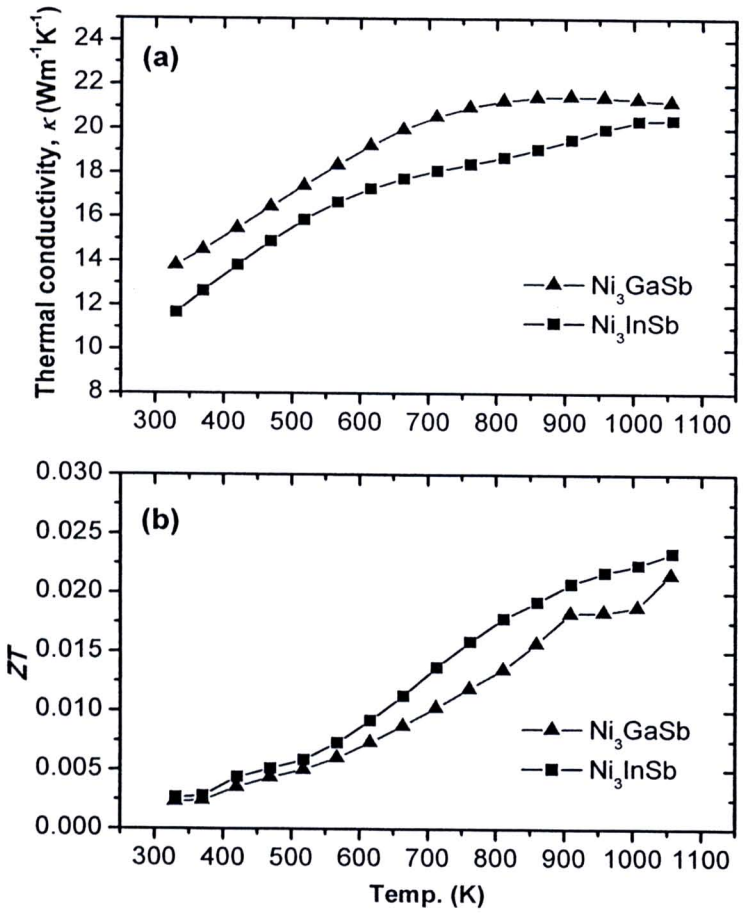

Figure 4.24 Temperature dependence of the (a) thermal conductivity κ, and (b) dimensionless Figure of Merit ZT of Ni_3GaSb and Ni_3InSb polycrystalline samples.

The temperature dependence of the thermal conductivity (κ) of Ni_3GaSb and Ni_3InSb polycrystalline samples is shown in Figure 4.24(a). Unfortunately, the κ values of both samples were quite high like metals, and increased with temperature. Ni_3GaSb presented the higher κ values than Ni_3InSb, because of the larger electronic contribution on κ of Ni_3GaSb than that on κ of Ni_3InSb. The lattice thermal conductivity κ_{lat} was obtained by subtracting the electronic thermal conductivity κ_{el} from the total measured thermal conductivity κ. The value of κ_{el} was calculated using $\kappa_{el} = L\sigma T$, where σ is the electrical conductivity ($= 1/\rho$) and L is the Lorentz number ($L = 2.45\times10^{-8}$ $W\Omega K^{-2}$). Room temperature values of the κ_{lat} for Ni_3GaSb and Ni_3InSb were 3.2 and 2.3 $Wm^{-1}K^{-1}$, respectively. They are relatively low κ_{lat} , which would be caused by their complex crystal structure containing a number of vacancies, as described previously. The heavier molecular weight of Ni_3InSb than that of Ni_3GaSb would lead to the lower κ_{lat} of Ni_3InSb than that of Ni_3GaSb. Note that the calculated κ_{el} exhibited larger values than the measured κ at high temperatures, i.e. $\kappa_{lat} < 0$. This is likely due to (1) the sample for measuring ρ and κ is not the same one. i.e. one is 3 mm × 3 mm × 15 mm for ρ measurement, the other is 10 mm × 10 mm × 1 mm for κ measurement, (2) at high temperature the Lorentz number ($L = 2.45\times10^{-8}$ $W\Omega K^{-2}$) may be not valid, and (3) there existed the difference in the experimental uncertainties between ρ and κ measurement. Figure 4.24(b) shows the temperature dependence of the dimensionless Figure of merit ZT of the Ni_3GaSb and Ni_3InSb samples. The ZT values of both samples increased with temperature and reached the maximum values of 0.022 and 0.023 at 1073 K for Ni_3GaSb and Ni_3InSb, respectively.